## Title

Synthesis, theoretical and experimental characterisation of thin film Cu2Sn1-x Ge x S3 ternary alloys (x = 0 to 1): Homogeneous intermixing of Sn and Ge

## Permalink

https://escholarship.org/uc/item/90j1v02m

## Authors

Robert, Erika VC
Gunder, René
de Wild, Jessica
et al.

## Publication Date

2018-06-01

## DOI

10.1016/j.actamat.2018.03.043

Peer reviewed

Acta Materialia 151 (2018) 125–136

Contents lists available at ScienceDirect

Acta Materialia

journal homepage: www.elsevier.com/locate/actamat

Full length article

# Synthesis, theoretical and experimental characterisation of thin film $Cu_2Sn_{1-x}Ge_xS_3$ ternary alloys ($x = 0$ to 1): Homogeneous intermixing of Sn and Ge

Erika V.C. Robert [a, *], René Gunder [b], Jessica de Wild [c], Conrad Spindler [a], Finn Babbe [a], Hossam Elanzeery [a], Brahime El Adib [d], Robert Treharne [e], Henrique P.C. Miranda [a, f], Ludger Wirtz [a], Susan Schorr [b], Phillip J. Dale [a]

[a] *Université du Luxembourg, Physics and Materials Science Research Unit, 41 rue du Brill, L- 4422 Luxembourg*
[b] *Helmholtz-Zentrum Berlin für Materialien und Energie, Hahn Meitner Platz 1, D -14109 Berlin, Germany*
[c] *IMEC, Kapeldreef 75, B – 3001 Heverlee, Belgium*
[d] *Luxembourg Institute of Science and Technology, 41 rue du Brill, L - 4422 Luxembourg*
[e] *University of Liverpool, Department of Physics, Oxford St, Liverpool L69 7ZE, UK*
[f] *Université Catholique de Louvain, Institute of Condensed Matter and Nanosciences (IMCN), Place Louis Pasteur 1, B – 1348 Louvain-la-Neuve, Belgium*

ARTICLE INFO

*Article history:*
Received 12 January 2018
Received in revised form
15 March 2018
Accepted 21 March 2018
Available online 2 April 2018

*Keywords:*
Inorganic materials
Semiconductors
Thin films
Alloys

## ABSTRACT

$Cu_2Sn_{1-x}Ge_xS_3$ is a p-type semiconductor alloy currently investigated for use as an absorber layer in thin film solar cells. The aim of this study is to investigate the properties of this alloy in thin film form in order to establish relationships between group IV composition and structural, vibrational and opto-electronic properties. Seven single phase $Cu_2Sn_{1-x}Ge_xS_3$ films are prepared from $x = 0$ to 1, showing a uniform distribution of Ge and Sn laterally and in depth. The films all show a monoclinic crystal structure. The lattice parameters are extracted using Le Bail refinement and show a linear decrease with increasing Ge content. Using density-functional theory with hybrid functionals, we calculate the Raman active phonon frequencies of $Cu_2SnS_3$ and $Cu_2GeS_3$. For the alloyed compounds, we use a virtual atom approximation. The shift of the main Raman peak from $x = 0$ to $x = 1$ can be explained as being half due to the change in atomic masses and half being due to the different bond strength. The bandgaps of the alloys are extracted from photoluminescence measurements and increase linearly from about 0.90 to 1.56 eV with increasing Ge. The net acceptor density of all films is around $10^{18}$ cm$^{-3}$. These analyses have established that the alloy forms a solid solution over the entire composition range meaning that intentional band gap grading should be possible for future absorber layers. The linear variation of the unit cell parameters and the band gap with group IV content allows composition determination by scattering or optical measurements. Further research is required to reduce the doping density by two orders of magnitude in order to improve the current collection within a solar cell device structure.

## 1. Introduction

Thin film photovoltaic technology is dominated by CdTe and $Cu(In,Ga)(S,Se)_2$ (CIGSSe)- based devices which have reached power conversion efficiencies above 22% [1,2]. Nevertheless, the toxicity of Cd and the cost of In have led to the development of alternative absorber layers such as $Cu_2Zn(Sn,Ge)(S,Se)_4$ (CZTGSSe). These contain the more abundant elements Zn and Sn, but the respective device efficiencies do not exceed 12.6% [3], also when alloyed with germanium (30% Ge, 9.4% [4]) or to a smaller extent, doped with additional Ge nanolayers (<25 nm, 11.8% [5]). The high open-circuit voltage deficit observable in CZTSSe devices is attributed to various harmful intrinsic properties such as a high Cu-Zn disorder or bandgap fluctuations [6] that are still under debate and also promote the quest for other Cu-based semiconductor materials with fewer elements and thus perhaps a reduced complexity. Observed as a secondary phase in CZTS due to its lower bandgap [7], the Zn-free $Cu_2SnS_3$ ternary showed a sufficient light absorption and required p-type character that highlighted it as

---

* Corresponding author.
*E-mail address:* erika.robert@uni.lu (E.V.C. Robert).

https://doi.org/10.1016/j.actamat.2018.03.043
1359-6454/

another potential absorber layer candidate on its own for p-n junction solar cells [8]. The ternary alloy $Cu_2Sn_{1-x}Ge_xS_3$ (CTGS) then emerged as another potential p-type absorber layer when group IV substitution of Sn by Ge was attempted [9]. First p-n devices based on this ternary alloy have reached power conversion efficiencies above 6% [9,10]. However, solar cells based solely on $Cu_2SnS_3$ (CTS) or $Cu_2GeS_3$ (CGS) are below 5% efficient for similar device structures [11–13]. The coexistence of Sn and Ge in the absorbers seems therefore to offer a possibility for improvement of device performance. Indeed the replacement of tin by germanium in CTS allows to widen the optical bandgap of the material from about 0.93 eV (pure CTS [8]) to 1.56 eV (pure CGS [14,15]), and thus also to tune opto-electronic properties. The challenge is now to systematically investigate the structural and opto-electronic properties of thin film CTGS over the complete $x = Ge/(Ge + Sn)$ compositional range.

Preliminary studies on $Cu_2Sn_{1-x}Ge_xS_3$ powders found a continuous solid solution over the entire range of $x$. Going from $x = 0$ to 1 [16] the lattice parameters all decreased and the optical band gap increased. However the generalisation of these results on powders to the properties of thin films requires further experimentation. The reason for this is that the powders were synthesised at 750 °C for 2 days and 1000 °C for 1 h allowing the Sn and Ge to homogenously distribute themselves. Thin films are usually synthesised at around 550 °C for shorter periods of time and this may be insufficient time and energy to evenly distribute the elements. The phenomenon of insufficient mixing is well known for thin $Cu(In,Ga)Se_2$ films prepared by selenisation of metallic precursors [17]. These films normally consist of a gallium rich bottom layer and an indium rich top layer leading to a strong gradient in the band gap through the depth [17]. Therefore any study of thin films of CTGS should consider the distribution of elements through the depth of the films.

There exist different crystal structures of both CTS and CGS materials when synthesised within typical thin film processing temperatures. There are different possibilities to arrange the Cu and group IV elements around sulphur anions in the unit cells of $Cu_2SnS_3$ and $Cu_2GeS_3$, which explains their polymorphism [18]. Bulk CTS and CGS form a monoclinic structure when prepared at 550 °C [19,20]. CTS and CGS thin films have also been reported to form cubic, tetragonal, triclinic or orthorhombic crystal structures depending on the synthesis conditions [14,21]. The different crystal structures lead to different fundamental properties, such as different bandgaps. The monoclinic crystal structure has been calculated to correspond to the most ordered and lowest energy structure for CTS [18] and also found in the absorber layers leading to the highest device efficiencies [9,12]. The monoclinic CGS polymorph also showed photoluminescence yield at the expected bandgap position while the cubic one had no measurable yield [14].

In this study we investigate seven different CTGS thin film compositions in order to compare their properties to those found in the powder study. An annealing temperature of 550 °C is used to produce thin films with the monoclinic structure relevant [14,22] for solar cell devices. The composition is varied from $x = 0$ to 1 to verify the solid solution character of the ternary alloy in thin film form. Grazing incidence X-ray diffraction (GI-XRD) at multiple incidence angles is additionally used to investigate any in-depth group IV gradient. Le Bail refinement of the diffractograms allows to determine the lattice parameters of the compound semiconductor which will be compared to those of the powder study. Experimental Raman spectra are compared with calculated spectra to confirm the good intermixing of the group IV elements. The optical band gap is extracted from photoluminescence spectra whilst doping type and concentration are estimated from capacitance-voltage measurements.

## 2. Experiment

The precursors used for the synthesis of CTGS films are stacks of Cu:Sn and Cu:Ge alloys, DC sputtered on a Mo-coated soda-lime glass (SLG) substrate. Each of the alloys is deposited via simultaneous sputtering from separate targets (Cu,Sn/Cu,Ge) on a substrate held at 100 °C. A small lateral composition gradient is obtained as the sample holder is not rotated during the sputtering process. A study of the overall lateral composition of the precursors with energy-dispersive X-ray (EDX) spectroscopy (EDX: Oxford Instruments INCA X-MAX, 20 keV) showed agreement between large magnification measurements on 120 $\mu m^2$ areas and several 1 $\mu m^2$ points in those surfaces showing the smooth germanium rich compositions with $x$ values around 0.80 and the respective smooth copper poor compositions with Cu/(Ge + Sn) around 0.75. These as-deposited rather Ge rich Cu:Sn-Cu:Ge precursor stacks are further cut into 2.5 $cm^2$ area pieces and subsequently annealed in a tubular furnace at 550 °C under 1 mbar of forming gas $H_2/N_2$ (10/90%). For all annealings the precursors are placed in a porous graphite box with 100 mg of elemental sulphur powder (S, 5N purity from Alfa Aesar). The box was previously exposed to SnS (SnS, 3N purity from MKNano) and GeS powders (GeS, 4N purity from Sigma Aldrich). Due to the high vapour pressures of GeS and SnS at temperatures above 200 °C [23], the desorption of GeS and SnS from the box walls and sample occur. The final composition after annealing thus depends critically upon the residual SnS and GeS leftovers from previous annealings.

On the other hand the pure CTS and CGS ternaries ($x = 0$ and $x = 1$) are produced by the annealing of single copper layers electrodeposited on a Mo substrate, similarly as in Ref. [23]. These annealings are done either in the presence of sulphur and germanium monosulphide powders (GeS, 2N purity from Sigma-Aldrich) for CGS, or sulphur and tin monosulphide powders (SnS, 3N purity from MKnano) for CTS. The composition of all resulting absorber layers is studied with wavelength-dispersive X-ray spectroscopy (WDX: Oxford Instruments INCA X-MAX, 20 keV) permitting to differentiate sulphur from molybdenum. The analysis is both done on ~60 $\mu m^2$ areas chosen arbitrarily on each sample and several 1 $\mu m^2$ points within these surfaces. The homogeneity observed across various hundreds of microns allows consecutive averaging of the large area measurements. SEM (Scanning Electron Microscope) cross-sectional images of the absorbers are also recorded to know the average thickness. Depth-resolved crystallographic analysis is performed by grazing incidence X-ray diffraction with fixed incidence angles $\alpha$ of 0.5, 3 and 6° (GI-XRD: Panalytical X'Pert Pro MPD diffractometer with Cu Kα radiation, $\lambda = 1.5406$ Å). The penetration depth $z$ is described by the depth at which the incident X-ray intensity drops to 1/e. Approximate X-ray penetration depths $z$ in CTS, CGS and CTGS under a grazing incidence geometry are calculated as a function of 2θ (angle between X-ray source and detector; $10 \leq 2\theta < 90°$) for the three incident angles $\alpha$ assuming a monoclinic structure with four formula units per unit cell. As described in Ref. [24]:

$$z = -\ln(1/e) \times 1/(\mu(1/\sin(\alpha) + 1/\sin(2\theta-\alpha)) \qquad (1)$$

with $\mu$ the total mass attenuation coefficient ($cm^2/g$). The mass attenuation coefficients are obtained by dividing the attenuation coefficients for each chemical element, obtained from existing databases (NIST), by the mass density. As calculation of the material density requires the unit cell volume, lattice parameters of the monoclinic CTS and CGS unit cells are taken from powder diffraction data [16]. A typical unit cell of monoclinic CTGS is presented in Fig. 1, where a, b, c, α, β and γ are the lattice constants [25].

As seen in Fig. 2, the lowest incident angle α of 0.5°allows an X-

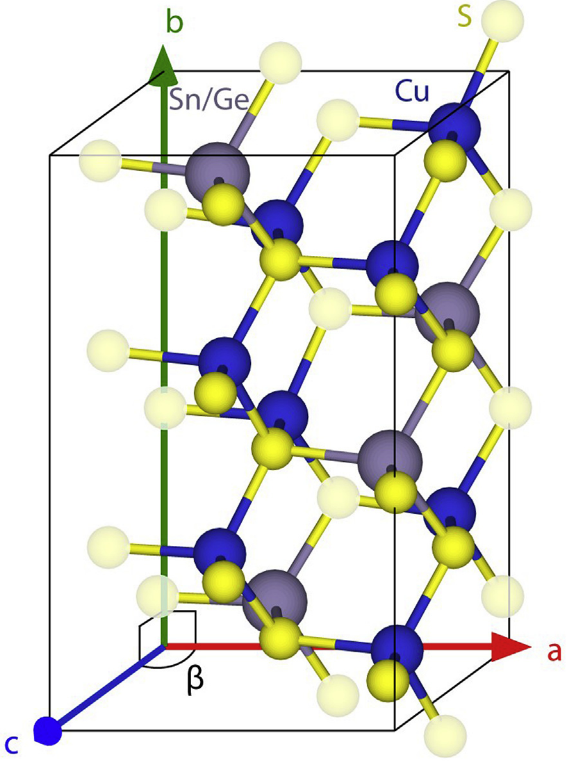

**Fig. 1.** Conventional unit cell of monoclinic CTGS (24 atoms) generated with the software Vesta [57] from lattice constants and atomic coordinates of CGS given in Ref. [25]. Orientation of the lattice is given by the (a,b,c)-coordinate system and adjacent sulphur atoms of neighbouring unit cells are marked in shaded yellow. (For interpretation of the references to colour in this figure legend, the reader is referred to the Web version of this article.)

ray penetration depth of less than 300 nm whilst for the highest angle of 6° the X-rays would reach up to 3 μm in the case of the low density CGS. The films are on average 2.4 μm thick as observed from cross-sectional scanning electron microscope images (not shown). Therefore $\alpha = 6°$ is required to extract the crystal information from depths closer to the Mo substrate. In order to calculate the lattice parameters a, b, c, and the angle β for the different compositions (as presented in Fig. 1 for the monoclinic lattice), the measured GI-XRD are all analysed by a Le Bail refinement using the FullProf Suite software and the Thompson-Cox Hastings pseudo-Voigt function for peak shape modeling. Details of the applied Le Bail procedure are described thoroughly in Ref. [24].

Raman measurements are performed on all samples with a Renishaw in-Via microRaman spectrometer and an excitation laser wavelength of 633 nm with a spot size of about 1 μm (5%, 30s integration time). Spots of 6 μm (50%, 60s) are also recorded to verify the large scale homogeneity (not shown). Additionally, photoluminescence measurements are performed with a home built setup at room temperature (RT-PL) equipped with a diode laser (660 nm excitation). The light with a spot diameter of 80 μm is dispersed with a 303 mm spectrograph and detected with a Si-CCD and an InGaAs-array detector. Apparent doping concentrations of the CTGS films are derived from capacitance-voltage (C- V) measurements. Aluminium (Al) was evaporated on the surface of the as-grown CTGS films (SLG/Mo/CGTS) using a Ferrotech Electron-beam evaporation tool for a thickness of 3 μm to provide a front contact. The SLG/Mo/CTGS/Al samples are then mounted in an evacuated cryostat at a temperature of 300 K under dark conditions for at least 8 h. After that, C-V measurements are performed using an Agilent E4980A Precision LCR Meter at a frequency of 100 kHz [26]. The apparent doping was extracted from the slope of a Mott-Schottky plot (plot of the inverse squared capacitance $1/C^2$ as a function of measured bias voltage V) [27,28].

## 3. Results

Seven $Cu_2(Sn_{1-x}Ge_x)S_3$ CTGS layers ($0 \leq x \leq 1$) are produced by annealing metallic precursors at 550 °C in the presence of SnS or GeS. The lateral composition of the seven CTGS layers is measured with WDX. The vapour pressure of the group IV sulfide (GeS or SnS) in the annealing atmosphere should have been sufficient to eliminate the small composition gradient present in the precursor [23]. The films need to be laterally homogeneous in order to evaluate if Ge/Sn depth gradients are present. In this aim lateral gradients should be ruled out both on a local and large area scale before any

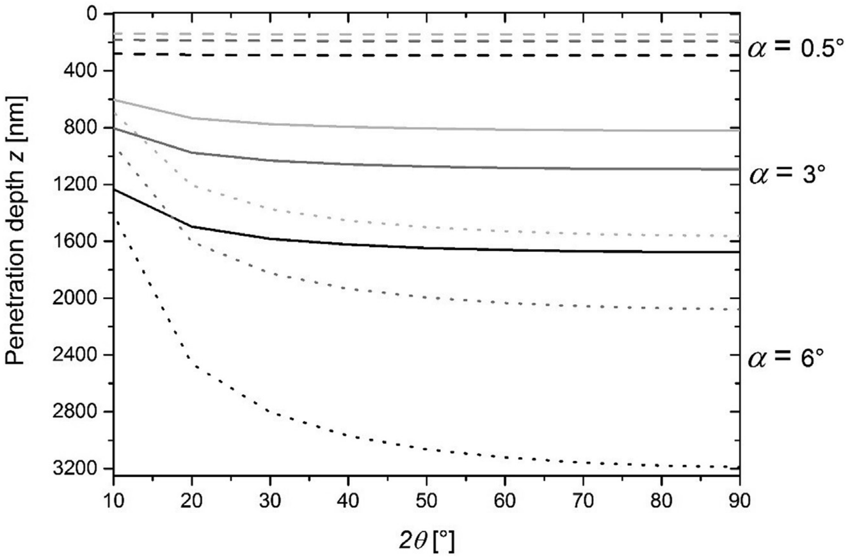

**Fig. 2.** X-ray penetration depth, $z$ (nm), calculated for pure CTS (light grey), a CTGS alloy ($x = 0.5$) (dark grey) and pure CGS (black) as function of $2\theta$. The calculation is done for grazing incidence geometry angles of $\alpha = 0.5$ (dashed lines), 3.0 (solid lines) and 6.0° (dotted lines), following the attenuation law [24].

further analysis is considered. Composition is thus evaluated both on micron-sized points and 60 $\mu m^2$ areas randomly over the surface of the sample. Compositional ratios in CTGS are defined as follows: $x = Ge/(Ge + Sn)$, $Cu/IV = Cu/(Ge + Sn)$ and $S/IV$ $(= S/Ge + Sn)$. WDX allows an elemental accuracy down to about ±1 at%. On each sample the variations of the elemental ratios; $\Delta x$, $\Delta(Cu/IV)$ and $\Delta(S/IV)$ are lower than 0.01, 0.03 and 0.09, respectively, which is below the WDX accuracy limits. Thus, the seven samples are considered as uniform and for each sample the compositional ratios are averaged over three large areas and reported in Table 1.

The final $x$ values reported in Table 1 demonstrate the successful synthesis of a series with various and increasing Sn substitution by Ge and are measured as 0; 0.24; 0.26; 0.43; 0.47; 0.63; 1. Cu/IV and S/IV ratio for the seven samples can be considered as identical being within the accuracy limits. All films are copper poor as $Cu/IV < 2$, which can be explained by the high partial pressure of SnS or GeS during the annealing [23]. Only in samples 1, 6 and 7 the sulphur amount is higher. This can be explained by the existence of pinholes within the layers uncovering the substrate and resulting in $MoS_2$ formation. Thus the S/IV ratio is higher in these areas since the group IV metals are absent. Evidence for an exposed substrate is found in the XRD of Fig. 3, and by a likely peak of $MoS_2$ seen in the Raman spectrum of sample 7 (cf.Fig. 8a), which shows the largest S/IV ratio.

The lateral compositional homogeneity of the films makes them suitable for studying any in-depth heterogeneity. GI-XRD was measured using incidence angles of $\alpha = 0.5$, 3 and 6° which probe between ~200 nm and 3 microns depth (as shown in Fig. 2). The most surface sensitive diffractograms, as measured with $\alpha = 0.5°$, are shown in Fig. 3 for the seven films. No contribution from the Mo substrate is expected with this low incident angle $\alpha = 0.5°$. Nevertheless, as mentioned in the EDX section and seen here, some of the samples ($x = 0.00$; 0.63 and 1) show the presence of Mo, suggesting the CTGS films are pinholed. It can be seen that except the peaks that relate to the Mo substrate, all peaks shift to higher $2\theta$ angles with increasing $x$. The direct comparison of measured data is made with theoretical diffractograms generated with the program PowderCell for all $x$ (shown in red in Fig. 3). PowderCell uses sets of lattice parameters, atomic coordinates and space group information to calculate X-ray diffractograms. The calculation is done assuming that both pure CTS and CGS materials obey a monoclinic structure with C1c1 space group [18] as expected from samples prepared under the same temperature conditions [23]. The atomic coordinates required for the calculation are taken from single crystal data [25,29]. The respective lattice parameters used, are shown in Table 2.

The lattice parameters a, b, c and β of CTGS alloys $(0 < x < 1)$ crystallised in the monoclinic C1c1 structure can be calculated assuming a linear decrease from CTS to CGS (i.e when $x$ increases from 0 to 1), in accordance with Vegard's law [24]. Values in Table 2 are taken as references for $x = 0$ and $x = 1$ ($\alpha = \gamma = 90°$ for all). The atomic coordinates are not known for the alloyed structures. The atomic coordinates of pure CGS [25] are used to generate theoretical XRD patterns for $0 < x < 1$, as it is sufficient to provide peak positions, ignoring minor errors in intensity ratio. Additional input of the site occupancy factor (SOF) as $x$ for Ge and $(1-x)$ for Sn in PowderCell takes into account the substitution of Sn by Ge.

**Table 1**
Compositional ratios $x = Ge/(Ge + Sn)$, $Cu/IV = Cu/(Ge + Sn)$ and $S/IV = S/Ge + Sn$ of the seven CTGS thin films under investigation.

| Sample | 1 | 2 | 3 | 4 | 5 | 6 | 7 |
|---|---|---|---|---|---|---|---|
| $x$ | 0.00 | 0.24 | 0.26 | 0.43 | 0.47 | 0.63 | 1.00 |
| Cu/IV | 1.95 | 1.83 | 1.94 | 1.94 | 1.98 | 1.84 | 1.86 |
| S/IV | 2.90 | 2.69 | 2.64 | 2.66 | 2.73 | 2.98 | 3.11 |

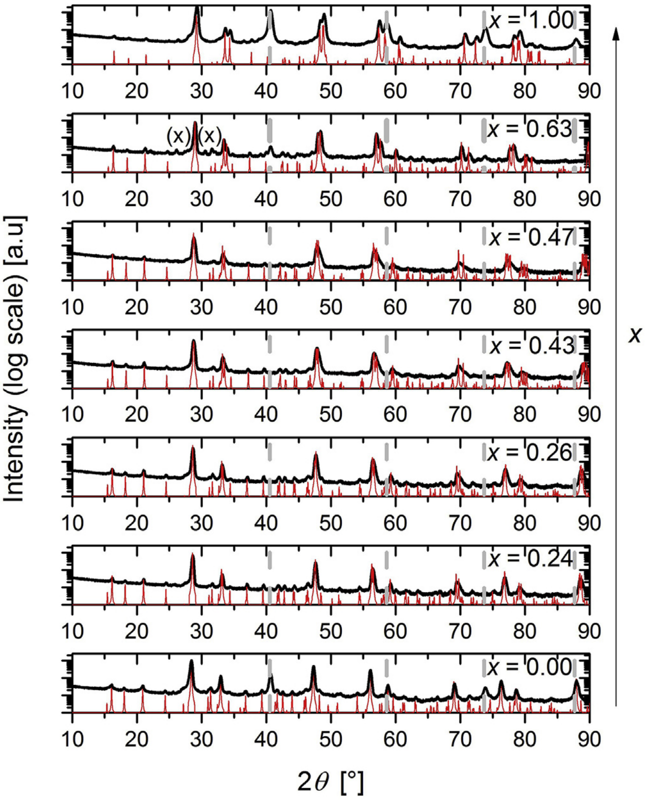

**Fig. 3.** Surface sensitive GI-XRD recorded with $\alpha = 0.5°$ on CTGS absorbers with $x = 0$; 0.24; 0.26; 0.43; 0.47; 0.63; 1 (as labelled on the graphs). The dashed grey lines indicate the Mo contribution (ICDD database: cubic, Im-3m, PDF 04-001-0059). Additional SnS peaks are shown by stars (x) (ICDD database: orthorhombic, Pbnm, PDF 00-039-0354). Theoretical patterns are generated with PowderCell for all $x$, and shown in red. The lattice parameters and atomic positions used for the calculation are taken from CTS ($x = 0$) and CGS ($x = 1$) data in the ICDD database (PDF 04-010-5719/PDF 04-010-4292) [25,29]. (For interpretation of the references to colour in this figure legend, the reader is referred to the Web version of this article.)

**Table 2**
Lattice parameters for monoclinic CTS and CGS (space group C1c1) used for generation of theoretical XRD patterns with PowderCell, as extracted from Refs. [29] and [25] with the estimated standard deviations in brackets.

| | a [Å] | b [Å] | c [Å] | β [°] |
|---|---|---|---|---|
| CTS [29] | 6.653(1) | 11.537(2) | 6.665(1) | 109.39(3) |
| CGS [25] | 6.449(2) | 11.319(3) | 6.428(2) | 108.37(2) |

As seen in Fig. 3, the CTS and CGS samples appear to be single phase monoclinic (with space group C1c1) because all measured peaks can be attributed either to it or to the Mo substrate. The same is true for the CTGS alloys with the only exception for $x = 0.63$ which shows two additional peaks (marked with (x)) which are most likely attributed to SnS. Additional small differences in intensity ratio between experimental and theoretical data could be attributed to the lack of exact atomic coordinates for all $x$. However, angular positions of the theoretical and experimental peaks are consistent. Using the atomic coordinates of pure CGS to generate the theoretical patterns was thus sufficient, showing the relative position of the atoms within the unit cell does not change drastically from CTS to CGS. The overall shift of the diffractogram peaks to higher $2\theta$ angles with increasing $x$ confirms the incorporation of Ge within the CTS structure: the most intense Bragg peak measured experimentally at ~28.4° in CTS (which is in fact an overlap of Bragg peaks 002, 231, 200) shifts to ~29.3° for pure CGS. The patterns for the five alloys are nearly identical but shift to higher angles $2\theta$ with increasing $x$. This all suggests that the monoclinic structure remains and only lattice parameters decrease with the inclusion of Ge, due to the lower ionic radius of $Ge^{+4}$ compared to the one of $Sn^{+4}$ (0.39 versus 0.55 Å [30]). For $x = 0.63$ and $x = 1.00$ an additional feature can be observed experimentally: the splitting of all the peaks with $2\theta = 33°$ (Bragg peaks 131 and $\bar{2}02$) into two visible peaks. The splitting is, however, present in all patterns generated with PowderCell for a CTGS monoclinic structure, the magnitude of the splitting becoming larger with increasing $x$. For germanium poor compositions the splitting is just too low to be resolved experimentally [14] and as seen in Fig. 3 the measured data supports this statement as the peaks are observed to broaden with increasing $x$.

### *3.1. Depth resolved XRD*

Depth resolved measurements were performed on all samples to investigate their uniformity from surface to bulk with respect to Ge gradients and secondary phases. Exemplary samples.

$x = 0.24$ and $x = 0.63$ are presented in Fig. 4. For $x = 0.24$ the CTGS Bragg peaks present in the first 300 nm ($\alpha = 0.5°$) are found at the same angular position $2\theta$ down to a depth of 3 microns ($\alpha = 3$ and 6°). No new reflections are observed through the depth. Only the intensity of the Mo peaks increases obviously with the incident angle, as the X-ray penetration depth increases within the sample. For $x = 0.63$ the angular positions of the CTGS peaks are also the same through the depth. The two minor peaks, corresponding to SnS, at the surface ($\alpha = 0.5°$) are not found in depth ($\alpha = 3$ and 6°). A slight contamination of SnS is thus only seen in the first 300 nm of that specific sample, which corresponds to about 10% of the total sample thickness (evaluated from cross-section imaging).

The diffractograms for the other $x$ values can be found in the supplementary material (S1). As for $x = 0.24$ in Fig. 4, they confirm the depth uniformity of the samples, with the presence of a single monoclinic (Cc) CTGS phase.

Visual inspection of the depth-resolved X-ray diffractograms in comparison with the theoretical patterns suggests the samples have a monoclinic crystal structure and are single phase (except for $x = 0.63$ which contains a little SnS in its first 300 nm, at most). Ge and Sn appear to be uniformly distributed both laterally and in depth, thus Le Bail refinement is performed on the full set of diffractograms to extract lattice parameters at all depths and confirm both the monoclinic structure and the compositional homogeneity. The absence of secondary phases in the samples suggests the existence of a solid solution of CTGS. SnS secondary phases have not been observed in powder samples grown in sealed quartz tubes [16]. Its slight presence here on the surface of the sample $x = 0.63$ is attributed to an impurity from the annealing environment. The lattice parameters a, b, c and β of the CTGS phase are refined on the basis of the monoclinic crystal structure (space group C1c1). Additionally both Mo and SnS-related reflections are refined when present, on the basis of a cubic structure for Mo (space group $Im\bar{3}m$) and an orthorhombic structure for SnS (space group Pbnm). In contrast to powder diffraction data previously performed on this material [16,31], thin film analysis presents an additional shoulder along with the main peak of CTGS (Bragg peaks 002, 231, 200) at about 28° in all samples (as seen in Fig. S2), with a broadening of the left hand side of the peak towards 27°. This feature suggests the presence of stacking faults in the Cu-poor CTGS films (Cu/IV < 2, cf. WDX data) as similarly observed in Cu-poor $CuInSe_2$ [32] (Cu/In < 1). The feature is thus selected as part of the background and not taken into account in the refinement. All GI-XRD experimental data for $\alpha = 0.5$, 3 and 6° is shown overlaid with respect to Le Bail fits in Fig. S3(1–21) of the supplementary material, as the overlay allows for the best judgement of the fit quality [33]. The resulting lattice parameters (LP), a, b, c and β, for the monoclinic CTGS at all $x$ are presented in Fig. 5 as function of the incidence angle ($\alpha = 0.5$, 3 and 6°) and in Fig. 6 as a function of $x$. Plotting the unit cell parameters as a function of $\alpha$ allows for an easy evaluation of any

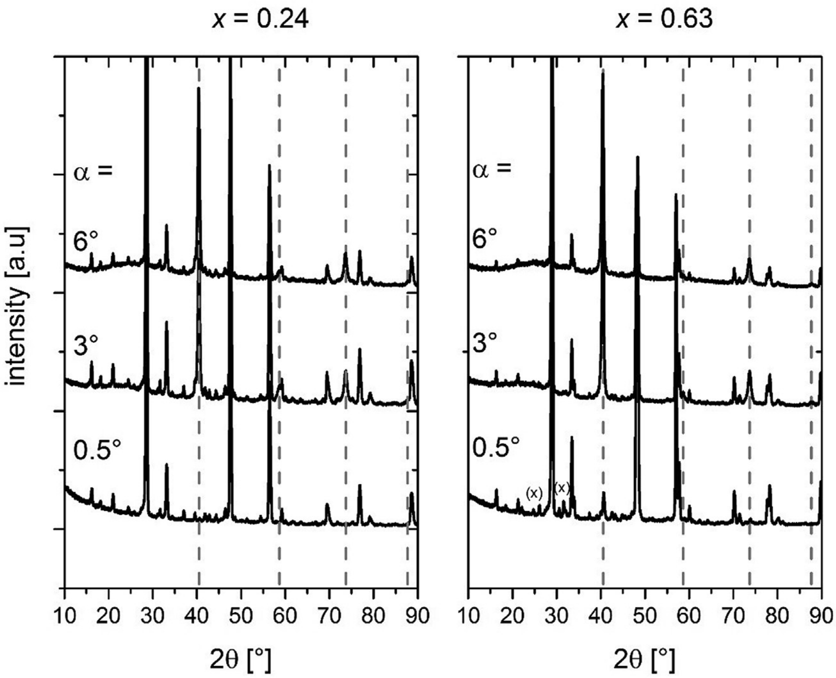

**Fig. 4.** Surface and bulk sensitive GI-XRD recorded with an incidence angle $\alpha = 0.5$, 3 and 6°(bottom to up) on the CTGS absorbers with $x = 0.24$ (left) and $x = 0.63$ (right). The dashed grey lines indicate the contribution of the Mo substrate (PDF 04-001-0056) and the stars (x) the minor SnS peaks (PDF 00-039-0354). The latter only appear at the surface of the sample $x = 0.63$.

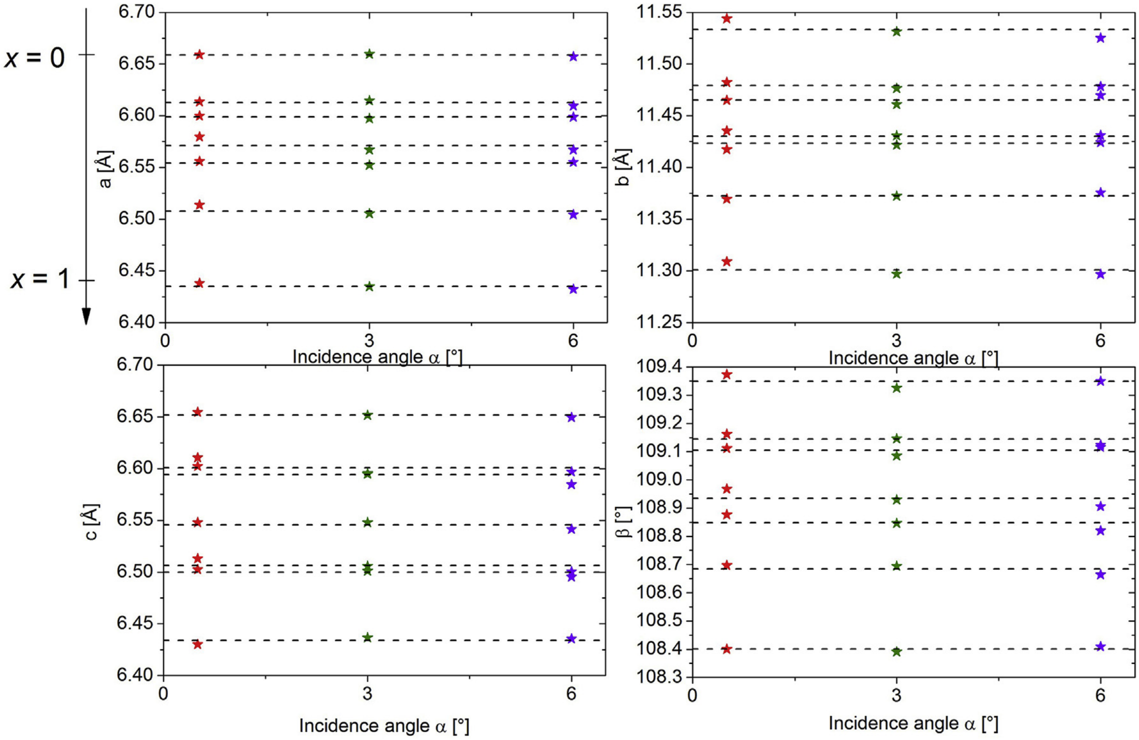

**Fig. 5.** Lattice parameters (a, b, c in Å and β in °) determined by Le Bail refinement on the depth resolved GI-XRD plotted as function of the incidence angle $\alpha$ used: 0.5° (red), 3° (green) and 6°(purple). The lattice parameters decrease with increasing $x$ from 0 to 1, as labelled. The dotted lines show the average of the three incidence angles for each $x$. The y-errors bars are smaller than the symbols, thus not shown. (For interpretation of the references to colour in this figure legend, the reader is referred to the Web version of this article.)

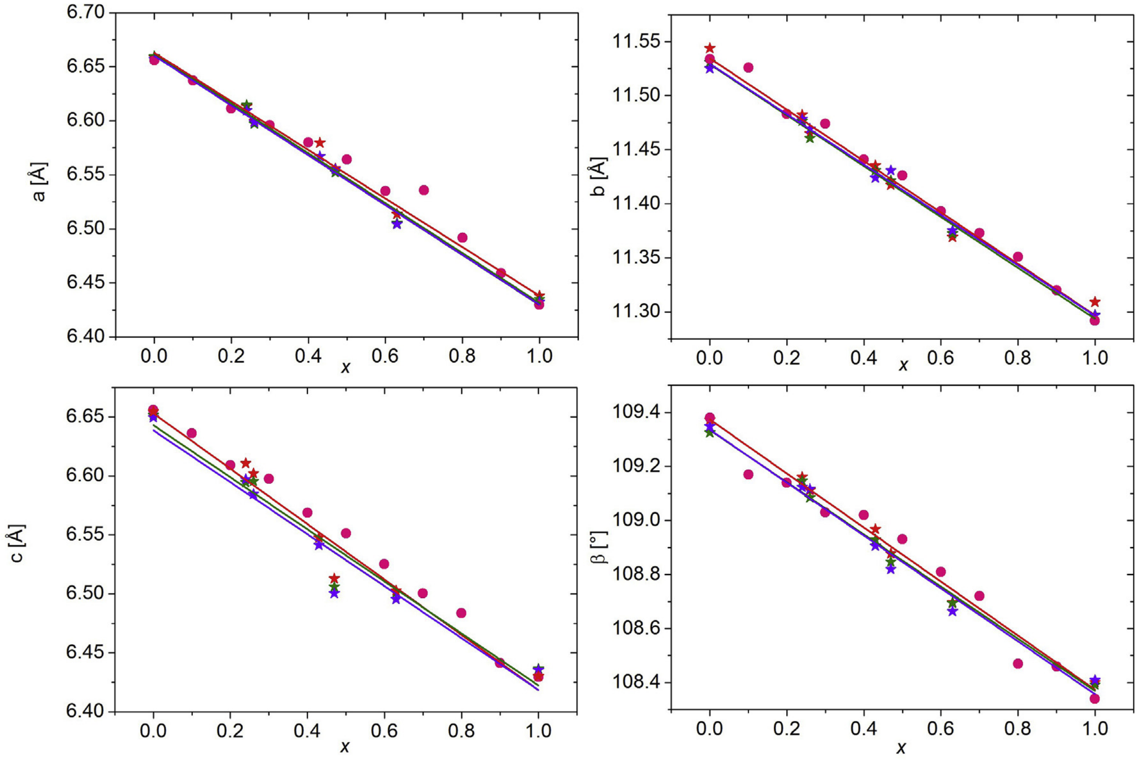

**Fig. 6.** Lattice parameters (a, b, c in Å and β in °, shown as stars) determined by Le Bail refinement on the depth resolved GI-XRD measured with $\alpha = 0.5$ (red), 3 (green) and 6°(purple) plotted as function of $x$. The straight lines are fit to the data as function of $x$, for each $\alpha$: 0.5°(red line), 3° (green line) and 6° (purple line). The direct comparison is drawn with extracted parameters from powder diffraction [16], shown as pink dots. The x and y-errors bars are smaller than the symbols, and thus are not shown. (For interpretation of the references to colour in this figure legend, the reader is referred to the Web version of this article.)

systematic variation in depth of the films. Here in Fig. 5 no trend is observed indicating a lack of compositional group IV gradient in the depth of the samples. This easy intermixing of the group IV elements, Sn and Ge, is different to what is observed for the popular Cu(In,Ga)$Se_2$ ternary alloy where In and Ga depth gradients are often observed [17]. Plotting the unit cell parameters as a function of $x$ in Fig. 6 allows to test for deviation away from Vegard's law [24]. For comparison the lattice parameters for the same material extracted from powder diffraction data [16] are also plotted in Fig. 6. The thin film data measured here is in agreement with the powder data and can be fitted with a straight line ‘LP = m$x$ + n’. Within error (cf. Table S1 for the complete dataset), the fits are the same for each $\alpha$, thus confirming the depth uniformity of the samples. The averaged fitting data is presented in Table 3. As Mo contributes to most of the diffractograms, its lattice parameters (a = b = c, $\alpha = \beta = \gamma = 90°$) are also refined within its known cubic structure and the resulting lattice constant ‘a’ is presented in Fig. S4. For $x = 0.63$ at $\alpha = 0.5°$ the orthorhombic SnS phase is added to the refinement, resulting in a = 3.99 Å, b = 11.19 Å and c = 4.30 Å with $\alpha = \beta = \gamma = 90°$, which fits with thePbnm space group (ICDD database).

The depth resolved Le Bail analysis in Figs. 5 and 6 show similar lattice parameters at all depths, which confirms the intermixing of Ge and Sn and the homogeneity of the crystalline structure. Additionally, a linear decrease of all lattice parameters is observed as expected with the inclusion of germanium due to a lower ionic radius than tin leading to shorter bond lengths on average. The lattice parameter values are in good agreement with lattice parameters determined previously from powder data [16]. No secondary phases were observed, meaning that there is a complete solid solution for all values of $x$.

### 3.2. Modelling of phonon modes

Raman spectroscopy is a complementary tool to XRD since it can probe surfaces locally down to dimensions of 1 micron square, and it may be more sensitive to secondary phases than XRD. Previously, experimental Raman spectra have been reported in the range of 250–400 $cm^{-1}$ showing 6 to 10 different modes [16,19,34,35]. The (primitive) unit cell of CTGS contains N = 12 atoms and therefore 3N-3 = 33 different phonon modes can be maximally expected in the spectra (according to group-theoretical analysis all modes are Raman-allowed). Therefore we calculate all the expected phonon modes for the CTGS alloy in order to be able to compare it with experimental spectra.

A precise calculation of phonons in an alloy of mixing parameter $x$ would imply the construction of a representative set of supercells with a ratio of Ge and Sn of $x$/(1-$x$). Such calculations quickly become unfeasible, in particular since we are using a hybrid functional. In order to better understand the shift of the Raman peaks from CTS to CGS as a function of the “mixing parameter” $x$, we have used the virtual crystal approximation, developed long time ago in the context of semi-empirical force-constant description of phonons [36,37]. This approximation enables us to interpolate the phonon frequencies between the pure compounds CTS and CGS. We start with ab-initio calculations of the optimized lattice geometries and the phonon frequencies of pure CTS and CGS. Standard density-functional theory (DFT) in the local density approximation (LDA) or generalized-gradient approximation (GGA) underestimates the bandgap and, for CTS and CGS, even yields an inverted bandgap. In previous phonon calculations of related materials [38], the LDA + U approximation was used in order to open the bandgap. We have also checked this approach, but found that the resulting frequencies are too low with respect to the experimental values. In particular, we would need to use different values of U for CGS and CTS, making a reliable comparison of phonon frequencies between the two materials difficult. We thus use the HSE06 hybrid functional [39] as in previous calculations [40] of the optical properties of these materials. Calculations were performed using VASP [41], using PAW potentials with an energy cutoff at 400 eV. A comparison of the optimized lattice parameters of CTS and CGS with the lattice parameters obtained from Le Bail refinement in Table 3, is shown in Table 4. The overall agreement is very good, in particular, the relative trends in lattice constants and bond angles between CTS and CGS are well reproduced by the calculations. Since with the DFT-HSE06 calculations, we reproduce both the electronic and structural properties, we expect that also the relative trends in phonon frequencies can be reliably reproduced. Furthermore, we confirm this by comparing with the experimental data.

**Table 3**
Average equations of linear fits of the lattice parameters (LP = m$x$ + n) presented in Fig. 6. Since all incidence angles lead to the same values within experimental error, the values were averaged. All equations can be found in Table S1.

| Lattice parameter LP | Slope m [Å or °] | y-intercept n [Å or °] |
|---|---|---|
| a | −0.229 | 6.662 |
| b | −0.235 | 11.531 |
| c | −0.225 | 6.645 |
| β | −0.981 | 109.348 |

The dynamical matrix is defined as the derivative of the force acting on atom $t$ in direction $j$ with respect to displacement $u$ of atom $s$ into direction $i$. We have calculated the dynamical matrices (for phonon wave vector $q = 0$) $D_{CTS}$ and $D_{CGS}$ of CTS and CGS, respectively, using finite differences as implemented in the phonopy package [42].

$$D^{ij}_{st}(\boldsymbol{q}) = \frac{\partial}{\partial u^{*i}_{s}(\boldsymbol{q})} F^{j}_{t}(\boldsymbol{q})$$

Phonon frequencies are then obtained by solving the secular equation,

$$\det\left|\frac{1}{\sqrt{m_s m_t}} D^{ij}_{st} - \omega^2\right| = 0$$

where $m_s$, $m_t$, denote the masses of atoms $s$ and $t$.

In order to obtain a good estimate of the phonon frequencies of the alloys, we use the “virtual crystal approximation” in which the original monoclinic crystal structure of CGS/CTS and the 12 atom unit cell are maintained. However, the dynamical matrix is interpolated as:

$$D(x) = xD_{CGS} + (1 - x)D_{CTS}.$$

In addition, we also interpolate the mass of the group IV atom as

$$m_{IV}(x) = xm_{Ge} + (1 - x)m_{Sn}.$$

In this way, the germanium atoms are continuously “converted” into tin atoms.

**Table 4**
Comparison of calculated lattice parameters using the HSE06 hybrid functional, with lattice parameters obtained by Le Bail refinement of experimental XRD data for any $\alpha$, in monoclinic CTS and CGS (space group C1c1).

| | a [Å] | b [Å] | c [Å] | β [°] |
|---|---|---|---|---|
| CTS calc./exp | 6.666/6.662 | 11.530/11.531 | 6.682/6.645 | 109.345/109.348 |
| CGS calc./exp | 6.450/6.433 | 11.288/11.296 | 6.429/6.420 | 108.523/108.367 |

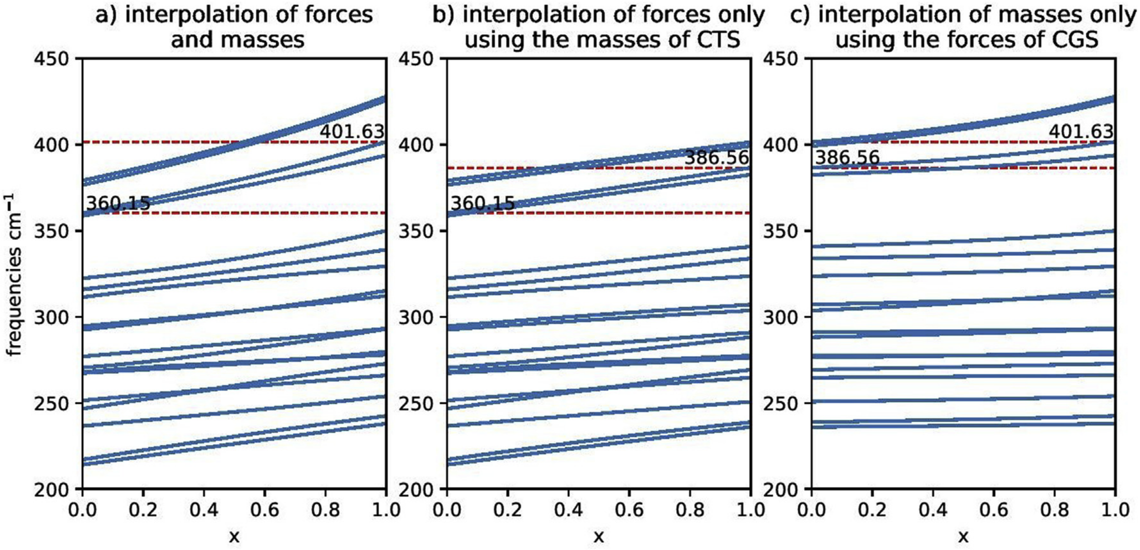

**Fig. 7.** Interpolation of phonon frequencies from CTS to CGS where the phonon frequencies of $Cu_2Sn_{1-x}Ge_xS_3$ are calculated in the virtual atom approximation as a function of $x$. (a) Interpolation of both dynamical matrix and atom masses, (b) interpolation of the dynamical matrix only with $m_{IV} = m_{Sn}$, (c) interpolation of the mass of the group IV atom only, using the dynamical matrix of CGS.

The resulting phonon frequencies are shown in Fig. 7. We show calculations where we continuously interpolate both the dynamical matrix and the masses (panel (a)) and where we just interpolate the dynamical matrix (panel (b)) or the mass of the group IV atom (panel (c)). In all three panels, we mark the minimum and maximum values of the phonon that gives rise to the maximum intensity peak in the Raman spectra. Between CTS and CGS this peak shifts by about 40 $cm^{-1}$ from 360.2 $cm^{-1}$ to 401.6 $cm^{-1}$. Roughly half of this shift can be attributed to a change in the strength of the chemical bond as one switches from a Sn-S to a Ge-S bond. The remaining half of the shift can be attributed to the change in mass from $m_{Sn}$ to $m_{Ge}$.

### 3.3. Comparison of Raman modelling and experiments

The sketch of the calculated Raman modes is presented in Fig. 8a) together with the experimental spectra of the thin films reported in Fig. 8b). The sketch assumes a uniform intensity and width of all 33 Raman active phonons (ab-initio calculations of resonant Raman intensities using hybrid functionals are currently not feasible). Details to access the scripts that were used to generate the calculated spectra can be found in section V of the supporting information. Table 5 reports the positions of the observed modes for $x = 0$ and $x = 1$ (pure CTS and CGS), together with values found in literature for the same compositions.

The theoretically calculated phonon sketch in Fig. 8a) contains 33 modes. Some of the modes are overlapping, leading to higher plotted peak intensities and less than 33 peaks. The significance of the higher peak intensity is to just show the mode overlaps, and may not correspond to the observed Raman peak intensities. The experimental Raman spectra show a fair comparison to the phonon sketch with identification of four separate regions of modes, although in the experiment (cf Fig. 8b)) the modes in region 2 have almost vanishing intensity. The experimental spectra also all have fewer peaks than the calculated phonon sketch (where all phonons contribute with equal intensity). The theoretical calculations simply show the possible phonon modes, but not their likely intensity. The calculations confirm the existence of the Raman modes measured between 50 and 100 $cm^{-1}$ in region 1, never reported previously. We also note the good agreement in the degree of peak shifting between theoretical and experimental data as $x$ increases from 0 to 1. For example the most intense mode in CTS at 353 $cm^{-1}$ shifts to 394 $cm^{-1}$ for CGS in Fig. 8b) revealing a shift to higher frequencies by about 40 $cm^{-1}$. This corresponds rather well to the theoretically expected shift of the main peak from 360.2 to 401.6 $cm^{-1}$ in Fig. 8a).

Examining regions 3 and 4 in Fig. 8b), the four modes observed in the CTS sample at frequencies between 290 and 450 $cm^{-1}$ were previously reported in literature for the monoclinic structure of CTS in both thin film [34] and powder [16] forms. Similarly the seven modes observed in the CGS sample at frequencies between 275 and 450 $cm^{-1}$ were also previously reported in the literature for a monoclinic structure in CGS bulk crystals [19,35] and/or powders [16], at the exception of the mode at 408 $cm^{-1}$ which was not reported previously but is visible in the spectra and likely relates to $MoS_2$ [43]. The presence of SnS suggested by XRD at the surface of the sample $x = 0.63$ is not observed with Raman spectroscopy (160 and 191 $cm^{-1}$ [44]) which could mean that it is in low concentration, or that it is preferentially orientated in such a way that its modes are not visible, as also seen by the lack of multiple reflections in XRD. Overall the experimental data suggest that – while the evolution with $x$ of most peaks at lower frequencies (regions 1, 2 and 3) seem to follow a one-mode behavior – the most intense mode in region 4 seems to follow rather a two-mode behavior [45]. Our interpolation model, however, only allows to describe a one-mode behavior. The two-mode behavior occurs when the (effective) masses or the force constants vary strongly between the alloy's constituents. In this case, the frequencies of the pure CTS and CGS compounds are so different that in the mixed compounds both phonon modes are visible. A complete dynamical study of the 2-mode behavior would imply modelisation of disordered alloys in supercells. This has, e.g., been done using the "random-element isodisplacement model" [36] for phonons in group-III nitride alloys [46,47]. This goes, however, beyond the scope of this manuscript, where we content ourselves to linearly interpolate between the pure materials CTS and CGS in order to disentangle the influence of the effective mass and of the chemical bond strength (force constants). Therefore, with this model, we do not claim to explain the 2-mode behavior (splitting of peaks) observed from CTS to CGS in section 4 of the spectra. Nevertheless, we get a rather complete

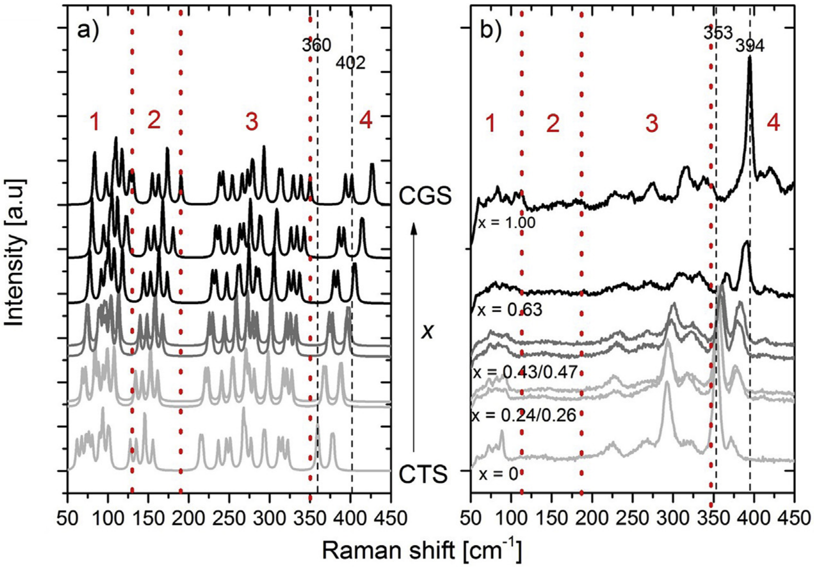

**Fig. 8.** a) Calculated vibrational spectra of CTGS in the virtual atom approximation for all $x$ plus one additional composition at $x = 0.8$, not produced experimentally. Each spectrum is y-shifted proportionally to its composition, in order to follow the peak shifts more easily. All phonon modes are represented by a Lorentzian peak with a width of 5 cm$^{-1}$ and unit height. The calculated phonon modes that correspond to the maximum intensity peaks of pure CTS and CGS in b) are indicated by vertical dashed lines. b) Raman spectra recorded on the full series of CTGS films with $x = 0$; 0.24; 0.26; 0.43; 0.47; 0.63; 1 (bottom to top, shaded from light grey to black). The same y-shift is applied as in a), for cross-comparison. The most intense modes in pure CTS and CGS are highlighted by the vertical black dashed lines. Four regions of modes are identified in both calculated and experimental data and separated by the red dashed lines. (For interpretation of the references to colour in this figure legend, the reader is referred to the Web version of this article.)

reproduction of the main peak positions in the four sections of the spectra.

### 3.4. Photoluminescence

Room temperature photoluminescence (RT-PL) measurements are performed on the sample series and the resulting spectra are shown in Fig. 9a). The wavelength of laser light excitation was 660 nm, which corresponds to a penetration depth of about 250 nm considering the absorption coefficient for CTGS of $4 \times 10^4$ cm$^{-1}$ [40]. Each spectrum shows a main peak (labeled $E_2$) at energies above 0.9 eV, whose maximum point is used for the normalisation. An additional peak labelled as $E_1$ is seen in all alloys at 0.9 eV, assigned to an unknown deep defect. Only $x = 0.63$ shows larger tailing and no $E_1$ but a feature around 0.9 eV (circled in red) related to water absorption [48]. For the pure ternaries $E_1$ appears to be shifted to lower energies.

The peak maximum of $E_2$ shifts to higher energies with the increase of Ge content in the films, until it reaches about 1.56 eV for the pure CGS sample. The band-to-band transition in pure monoclinic CGS was previously evaluated to 1.50–1.59 eV from both photoluminescence and absorption data on thin films and bulk crystals [14,15,35]. The peak maximum of $E_2$ for $x = 0$ (pure CTS) cannot be evaluated accurately since it overlaps with defect luminescence at 0.8 eV. Only an approximate value of 0.90–0.94 eV can be extracted for the maximum of $E_2$. The band-to-band transition of pure CTS was determined for monoclinic samples to be around 0.93–0.95 eV [8,22]. Theoretical calculations of the absorption onsets matched these experimental values [40]. Therefore, since it dominates at room temperature for each $x$, the peak $E_2$ for each $x$ is assumed to correspond to the band-to-band transition.

**Table 5**
Raman modes measured and observed in Fig. 8b) together with the modes previously reported in literature, for pure CTS and CGS.

| CTS [34] | CTS [15] | | CTS in this work |
|---|---|---|---|
| | | | 58, 64, 73, 81, 89, 226 |
| 290 | 292 | | 292 |
| 314 | 319 | | 319 |
| 352, 374 | 355, 373 | | 353, 371 |
| CGS [35] | CGS [19] | CGS [16] | CGS in this work |
| | | | 60, 72, 84, 94, 106, 112, 227, 249 |
| | 275 | 276 | 275 |
| | 296 | 292 | |
| 321, 339 | 320,348 | 319, 340 | 315, 338 |
| | | 355 | |
| | | 373 | 371 |
| 396 | 397 | 397 | 394 |
| | | | 408 ($MoS_2$) |
| 421, 427 | 420 | 424 | 419> |

Returning to the question if SnS is really present in the film with $x = 0.63$, a photoluminescence peak around 1.3 eV [49] due to its band-to-band transition might be observable. However, for this sample it would likely overlap with the band-to-band transition from the CTGS itself.

Both monoclinic CTS and CGS materials are characterised by a split valence band, where the second valence band lies at a maximum of 200 meV below the first, as observed in light absorption measurements and confirmed by theoretical calculations [22,40,50–52], which means it could also be observed on the right hand side of the PL maximum $E_2$. As no significant feature is observed above $E_{2,}$ we consider the intrinsic valence band splitting does not affect $E_{2.}$

For an ideal material with no tail state, the bandgap energy $E_g$ can be extracted from the peak maximum $E_{max}$ of the band-to-band transition related peak $E_2$ [53], following:

$$E_g = E_{max} - ½\, k_B\, T$$

where $1/2 k_B T \sim 12.9$ meV at room temperature (T = 298 K) with $k_B$ the Boltzmann constant. However, the presence of a high density of tail states, as in CZTSSe [53], is known to redshift the value of $E_{max}$, leading to an underestimation of $E_g$ by hundreds of meV. The importance of tailing in CTGS can be checked by comparing the

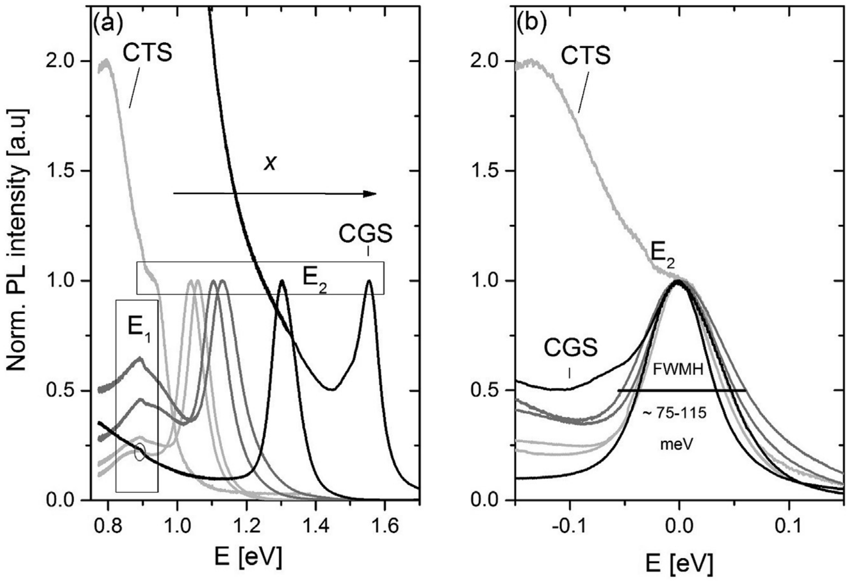

**Fig. 9.** (a) PL spectra normalized to the peak maximum $E_2$, highlighted in rectangle for all $x$ ($0 \leq x \leq 1$, with shading from light grey for $x = 0$ to black for $x = 1$). The luminescence peak $E_1$ is also highlighted for $0 < x < 1$ in a separate vertically orientated rectangle. Only $x = 0.63$ shows large tailing and no $E_1$ but a feature around 0.9 eV (circled in red) related to water absorption [48]. (b) Overlay of all normalized PL spectra shifted by their maximum $E_{max}$ for comparison of peak widths (FWHM). (For interpretation of the references to colour in this figure legend, the reader is referred to the Web version of this article.)

peak widths of the main peak $E_2$. For this purpose the spectra are shifted by their respective bandgap and the radiative peaks are overlaid and plotted in Fig. 9b). Not considering $E_2$ peaks for the pure CTS and CGS materials that strongly overlap with sub-bandgap luminescence, the FWHM values can be estimated to be between about 75 and 115 meV. The absorption model for fitting PL data with strong tailing described in Ref. [54] demonstrates that FWHM ~ 70–120 meV does not significantly alter the position of peak maxima $E_{max}$, only underestimating $E_g$ by about 20 meV. Therefore, using the peak maximum $E_{max}$ of $E_2$ as an estimation for $E_g$ only leads to a maximum error of 20 meV.

The extracted bandgaps from $E_2$ are represented in Fig. 10 together with the values extracted from transmission-reflectance measurements on powder samples [16]. Theoretical bandgaps for pure CTS, pure CGS and $x = 0.5$ are also added for comparison, from two different sources, the first taking into account the intrinsic valence band splitting and the second not [40,55]. Bandgaps extracted from thin film data increase linearly with $x$ as $E_g = 0.643x + 0.906$, in agreement with bandgaps measured and calculated for pure CTS and pure CGS [40]. However the bandgaps from the thin film study are all higher than those found in the powder study by about 50 meV. Light absorption measurements are known in such materials to underestimate bandgap values [14], and care should be taken in evaluating the bandgap from the different existing onsets due to the valence band splitting [40].

According to the Shockley Queisser limit the highest power conversion efficiencies for single junction solar cell devices are achieved with an absorber layer band gap of between 1.15 and 1.35 eV. For CTGS this would correspond to values of approximately $0.4 < x < 0.7$.

### 3.5. Electrical measurements

In order to investigate the electrical properties of the alloys, aluminium front contacts were added to the films and capacitances were measured for different applied bias. Mott-Schottky plots ($1/C^2 \propto V$) allow for determination of doping type and concentration. The doping concentration corresponds to the slope of the linear fit to the measured data. All samples showed a linear response except for the pure CTS sample ($x = 0$) which could not be evaluated since the sample was electrically shunted due to a high number of pinholes. Fig. 11 shows the Mott-Schottky plot evaluated for $x = 0.24$. The negative slope confirms the p-type character of the films, and is thus suitable for creation of pn junction photovoltaic devices. However, the apparent net doping concentration, $N_A$, is in the order of $10^{17} cm^{-3}$ for this sample. Doping concentrations for all $x$ (except $x = 0$) are reported in Table 6. $N_A$ varies from 4 to $35 \times 10^{17}$ $cm^{-2}$

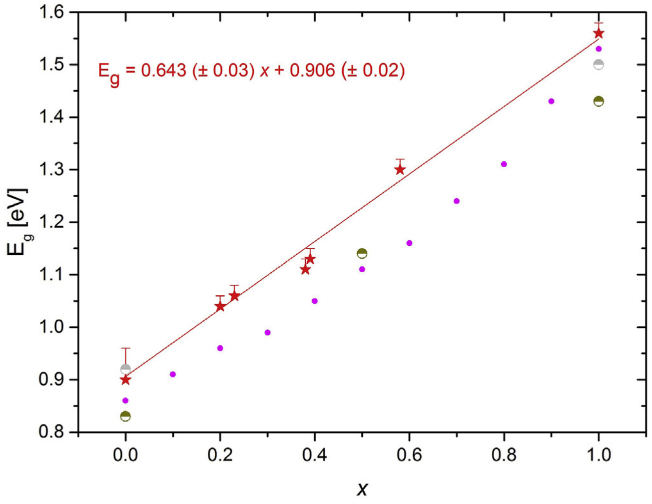

**Fig. 10.** Bandgap energies $E_g$ (red stars) extracted from the PL peak maximum $E_2$ for all $x$, plotted together with the $E_g$ extracted from light transmission-reflection measurements on CTGS powder samples (pink dots) [16]. A linear fit is performed and the equation shown on the graph. Using the maximum of $E_2$, $E_g$ is underestimated by 20 meV only (error bars). Only the error on CTS is a bit larger due to the PL tailing. Additionally theoretical bandgaps from Ref. [40] are shown as half-filled grey circles for pure CTS, CGS and [55] as half-filled green circles for pure CTS, CGS and $x = 0.5$. The x-errors are smaller than the symbols, and are thus not shown. (For interpretation of the references to colour in this figure legend, the reader is referred to the Web version of this article.)

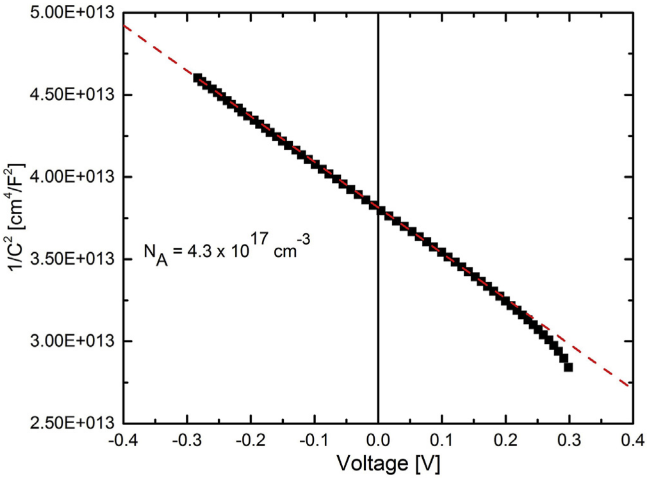

**Fig. 11.** Exemplary Mott-Schottky plot $1/C^2 \propto V$ measured on the sample with $x = 0.24$ whose slope is used to extract the doping density $N_A$.

with no clear trend with respect to neither the group IV composition nor the individual Cu/IV or S/IV ratios.

Baranowski et al. showed for CTS that the lowest doping densities could be achieved by growing the material under Cu and S poor conditions [56]. Here the lowest doping density was also measured for $x = 0.24$, the sample with the least Cu or S. However, there is no clear trend amongst the other samples. Doping concentrations below $10^{18}$ cm$^{-3}$ are estimated in two of the films here, consistent with the work of Baranowski et al. [56] but remain at least one order of magnitude too high for achieving a large space charge width in typical p-n junction thin film photovoltaic devices.

## 4. Conclusion

Thin films of the $Cu_2Sn_{1-x}Ge_xS_3$ ternary alloy were successfully synthesised for various $x$ between zero and one, with complete intermixing of Sn and Ge, demonstrating the existence of a solid solution. The films all show a monoclinic structure from X-ray diffraction with uniform Ge-Sn intermix in the depth of the film. All films are single phase, with the exception of one which shows small signs of SnS at the surface, as concluded from the GI-XRD data, but it is not observed by other techniques. Le Bail refinement of the diffraction data showed the lattice parameters of the monoclinic unit cell evolved linearly as a function of $x$ the group IV composition. Phonon modes were calculated in CTGS and showed a similar degree of peak shifting with increasing Ge content as in the measured Raman spectra, thus confirming that the samples are single phase. We have disentangled the effect of atomic masses and of chemical bonds on the shift of the Raman peaks as a function of $x$. Comparison with the experimental data suggest that most Raman peaks display a one-mode behavior except for the most intense peak at high frequencies that shows a two-mode behavior. This could be used in the future to get more accurate insight into the alloying of CTGS.

Furthermore photoluminescence measurements give the bandgaps of the various alloys, with a linear increase from about 0.90 to 1.56 eV. Electrical capacitance measurements showed the films are p-type but their apparent net doping density is one to two orders of magnitude too high for device implementation. Future work on this semiconductor for photovoltaic applications should focus on reducing and controlling the doping density down to values near $10^{16}$ cm$^{-3}$. For copper chalcogenide semiconductors this is normally achieved by controlling the copper concentration. Additionally the composition should be between $x = 0.4$ and 0.7 since this corresponds to band gaps of 1.15 and 1.35 eV which are required for the maximum power conversion efficiency. Finally, bandgap grading for improved carrier collection should be possible from the perspective that no secondary phase segregation is expected.

**Table 6**
Report of apparent doping concentrations $N_A$ [cm$^{-3}$] estimated from C-V measurements.

| Sample | 1 | 2 | 3 | 4 | 5 | 6 | 7 |
|---|---|---|---|---|---|---|---|
| $x$ | 0.00 | 0.24 | 0.26 | 0.43 | 0.47 | 0.63 | 1.00 |
| $N_A \times 10^{17}$[cm$^{-3}$] | – | 4 | 22 | 8 | 35 | 11 | 18 |

## Acknowledgments

We acknowledge support from the National Research Fund, Luxembourg, through the EATSS project under the grant agreement C13/MS/5898466 and through project C12/MS/3987081/TSDSN (L.W. and H.P.C.M.). The Laboratory for Photovoltaics and the Laboratory of Energy Materials at the University of Luxembourg are fully acknowledged for help and discussion, especially Dr. Michele Melchiorre and Daniel Siopa for performing the majority of the WDX measurements. The working group of Structure and Dynamics of Energy Materials at the HZB is acknowledged for access and help with the measurements in the X-Ray CoreLab. Dr Inmaculada Pera Alonso is acknowledged for her complementary advice on the Le Bail refinements.

## Appendix A. Supplementary data

Supplementary data related to this article can be found at https://doi.org/10.1016/j.actamat.2018.03.043.

## References

[1] R. Kamada, T. Yagioka, S. Adachi, A. Handa, K.F. Tai, T. Kato, H. Sugimoto, New world record Cu(In, Ga)(Se, S)$_2$ thin film solar cell efficiency beyond 22%, in: 2016 IEEE 43rd Photovoltaic Specialists Conference (PVSC), 2016, pp. 1287–1291.

[2] R. Martin, First Solar's cells break efficiency record, MIT Technol. Rev. (2016). Available online, https://www.technologyreview.com/s/600922/.

[3] W. Wang, M.T. Winkler, O. Gunawan, T. Gokmen, T.K. Todorov, Y. Zhu, D.B. Mitzi, Device characteristics of CZTSSe thin-film solar cells with 12.6% efficiency, Advanced Energy Materials 4 (2014) 1301465.

[4] C.J. Hages, S. Levcenco, C.K. Miskin, J.H. Alsmeier, D. Abou-Ras, R.G. Wilks, M. Bar, T. Unold, R. Agrawal, Improved performance of Ge-alloyed CZTGeSSe thin-film solar cells through control of elemental losses, Prog. Photovoltaics 23 (2015) 376–384.

[5] S. Giraldo, E. Saucedo, M. Neuschitzer, F. Oliva, M. Placidi, X. Alcobe, V. Izquierdo-Roca, S. Kim, H. Tampo, H. Shibata, A. Perez-Rodriguez, P. Pistor, How small amounts of Ge modify the formation pathways and crystallization of kesterites, Energy Environ. Sci. 11 (2018) 582–593.

[6] S. Bourdais, C. Choné, B. Delatouche, A. Jacob, G. Larramona, C. Moisan, A. Lafond, F. Donatini, G. Rey, S. Siebentritt, A. Walsh, G. Dennler, Is the Cu/Zn disorder the main culprit for the voltage deficit in kesterite solar cells? Adv. Energy Mater. 6 (2016) 1502276.

[7] D.M. Berg, M. Arasimowicz, R. Djemour, L. Gütay, S. Siebentritt, S. Schorr, X. Fontané, V. Izquierdo-Roca, A. Pérez-Rodriguez, P.J. Dale, Discrimination and detection limits of secondary phases in $Cu_2ZnSnS_4$ using X-ray diffraction and Raman spectroscopy, Thin Solid Films 569 (2014) 113–123.

[8] D.M. Berg, R. Djemour, L. Guetay, G. Zoppi, S. Siebentritt, P.J. Dale, Thin film solar cells based on the ternary compound $Cu_2SnS_3$, Thin Solid Films 520 (2012) 6291–6294.

[9] M. Umehara, Y. Takeda, T. Motohiro, T. Sakai, H. Awano, R. Maekawa, $Cu_2Sn_{1-x}Ge_xS_3$ (x=0.17) thin-film solar cells with high conversion efficiency of 6.0%, APEX 6 (2013).

[10] M. Umehara, S. Tajima, Y. Aoki, Y. Takeda, T. Motohiro, $Cu_2Sn_{1-x}Ge_xS_3$ solar cells fabricated with a graded bandgap structure, APEX 9 (2016) 072301.

[11] X. Jin, L. Zhang, G. Jiang, W. Liu, C. Zhu, High open-circuit voltage of ternary $Cu_2GeS_3$ thin film solar cells from combustion synthesized Cu-Ge alloy, Sol. Energy Mater. Sol. Cell. 160 (2017) 319–327.

[12] M. Nakashima, J. Fujimoto, T. Yamaguchi, M. Izaki, $Cu_2SnS_3$ thin-film solar cells fabricated by sulfurization from NaF/Cu/Sn stacked precursor, APEX 8 (2015).

[13] A. Kanai, K. Toyonaga, K. Chino, H. Katagiri, H. Araki, Fabrication of $Cu_2SnS_3$ thin film solar cells with power conversion efficiency over 4%, in: WCPEC 2014, 6th World Conference on Photovoltaic Energy Conversion, Japan, Kyoto, 2014.

[14] E.V.C. Robert, J. de Wild, D. Colombara, P.J. Dale, Crystallographic and opto-electronic properties of the novel thin film absorber $Cu_2GeS_3$, in: Proc. SPIE 9936, Thin Films for Solar and Energy Technology VIII, 2016, p. 993607.

[15] H. Araki, K. Chino, K. Kimura, N. Aihara, K. Jimbo, H. Katagiri, Fabrication of $Cu_2GeS_3$-based thin film solar cells by sulfurization of Cu/Ge stacked precursors, Jpn. J. Appl. Phys. 53 (2014), 05FW10.

[16] H. Araki, M. Yamano, G. Nishida, A. Takeuchi, N. Aihara, K. Tanaka, Synthesis and characterization of $Cu_2Sn_{1-x}Ge_xS_3$, Phys. Status Solidi C 14 (6) (2017).

[17] J.C. Malaquias, D.M. Berg, J. Sendler, M. Steichen, N. Valle, P.J. Dale, Controlled bandgap $CuIn_{1-x}Ga_x(S_{0.1}Se_{0.9})_2$ $(0.10 \leq x \leq 0.72)$ solar cells from electro-deposited precursors, Thin Solid Films 582 (2015) 2–6.

[18] Y.-T. Zhai, S. Chen, J.-H. Yang, H.-J. Xiang, X.-G. Gong, A. Walsh, J. Kang, S.-H. Wei, Structural diversity and electronic properties of $Cu_2SnX_3$ (X = S, Se): a first-principles investigation, Phys. Rev. B 84 (2011).

[19] Y. Matsumoto, N. Aihara, N. Saito, K. Tanaka, Growth of $Cu_2GeS_3$ bulk single crystals by chemical vapor transport with iodine, Mater. Lett. 194 (2017) 16–19.

[20] Y. Matsumoto, N. Aihara, A. Munemura, K. Tanaka, Preparation of monoclinic $Cu_2SnS_3$ single crystal by chemical vapor transport with iodine, Mater. Lett. 170 (2016) 213–216.

[21] P.A. Fernandes, P.M.P. Salome, A.F. da Cunha, A study of ternary $Cu_2SnS_3$ and $Cu_3SnS_4$ thin films prepared by sulfurizing stacked metal precursors, J. Phys. D Appl. Phys. 43 (2010).

[22] J. de Wild, E.V.C. Robert, B.E. Adib, D. Abou-Ras, P.J. Dale, Secondary phase formation during monoclinic Cu2SnS3 growth for solar cell application, Sol. Energy Mater. Sol. Cell. 157 (2016) 259–265.

[23] E.V.C. Robert, J. De Wild, P.J. Dale, Reaction chemistry of group IV copper chalcogenide semiconductors $Cu_2MX_3$ (M = Sn, Ge and X = S, Se), J. Alloy. Compd. 695 (2017) 1307–1316.

[24] M. Dimitrievska, A. Fairbrother, R. Gunder, G. Gurieva, H. Xie, E. Saucedo, A. Perez-Rodriguez, V. Izquierdo-Roca, S. Schorr, Role of S and Se atoms on the microstructural properties of kesterite $Cu_2ZnSn(S_xSe_{1-x})_4$ thin film solar cells, Phys. Chem. Chem. Phys. 18 (2016) 8692–8700.

[25] L.M. de Chalbaud, G.D. Delgado, J.M. Delgado, A.E. Mora, V. Sagredo, Synthesis and single-crystal structural study of $Cu_2GeS_3$, Mater. Res. Bull. 32 (1997) 1371–1376.

[26] F. Werner, T. Bertram, J. Mengozzi, S. Siebentritt, What is the dopant concentration in polycrystalline thin-film $Cu(In,Ga)Se_2$? Thin Solid Films 633 (2017) 222–226.

[27] S.M. Sze, K.K. Ng, Physics of Semiconductor Devices, third ed., Wiley India Pvt. Limited, 2008.

[28] L. Van Puyvelde, J. Lauwaert, P.F. Smet, F. Pianezzi, S. Buecheler, S. Nishiwaki, A.N. Tiwari, H. Vrielinck, Deep level transient spectroscopy measurements on $Mo/Cu(In,Ga)Se_2$/metal structure, Thin Solid Films 582 (2015) 371–374.

[29] M. Onoda, X.A. Chen, A. Sato, H. Wada, Crystal structure and twinning of monoclinic $Cu_2SnS_3$, Mater. Res. Bull. 35 (2000) 1563–1570.

[30] R.D. Shannon, Revised effective ionic radii and systematic studies of inter-atomic distances in halides and chalcogenides, Acta Crystallogr. A 32 (1976) 751–767.

[31] F. Neves, J.B. Correia, K. Hanada, L.F. Santos, R. Gunder, S. Schorr, Structural characterization of $Cu_2SnS_3$ and $Cu_2(Sn,Ge)S_3$ compounds, J. Alloy. Compd. 682 (2016) 489–494.

[32] H. Stange, S. Brunken, H. Hempel, H. Rodriguez-Alvarez, N. Schäfer, D. Greiner, A. Scheu, J. Lauche, C.A. Kaufmann, T. Unold, D. Abou-Ras, R. Mainz, Effect of Na presence during $CuInSe_2$ growth on stacking fault annihilation and electronic properties, Appl. Phys. Lett. 107 (2015) 152103.

[33] B. Toby, R Factors in Rietveld Analysis: How Good Is Good Enough, 2006.

[34] D.M. Berg, R. Djemour, L. Guetay, S. Siebentritt, P.J. Dale, X. Fontane, V. Izquierdo-Roca, A. Perez-Rodriguez, Raman analysis of monoclinic $Cu_2SnS_3$ thin films, Appl. Phys. Lett. 100 (2012).

[35] N. Aihara, Y. Matsumoto, K. Tanaka, Photoluminescence characterization of $Cu_2GeS_3$ bulk crystals, Phys. Status Solidi B 254 (2017).

[36] I.F. Chang, S.S. Mitra, Long wavelength optical phonons in mixed crystals, Adv. Phys. 20 (1971) 359–404.

[37] R. Braunstein, A.R. Moore, F. Herman, Intrinsic optical absorption in germanium-silicon alloys, Phys. Rev. 109 (1958) 695–710.

[38] N.B.M. Amiri, A. Postnikov, Secondary phase $Cu_2SnSe_3$ vs. kesterite $Cu_2ZnSnSe_4$: similarities and differences in lattice vibration modes, J. Appl. Phys. 112 (2012) 033719.

[39] J. Heyd, G.E. Scuseria, M. Ernzerhof, Hybrid functionals based on a screened Coulomb potential, J. Chem. Phys. 118 (2003) 8207–8215.

[40] J. de Wild, E. Kalesaki, L. Wirtz, P.J. Dale, Valence band splitting in Cu2(Sn,-Ge,Si)S3: effect on optical absorption spectra, Phys. Status Solidi Rapid Res. Lett. 11 (2017) 1600410.

[41] G. Kresse, J. Furthmüller, Efficiency of ab-initio total energy calculations for metals and semiconductors using a plane-wave basis set, Comput. Mater. Sci. 6 (1996) 15–50.

[42] A. Togo, I. Tanaka, First principles phonon calculations in materials science, Scripta Mater. 108 (2015) 1–5.

[43] É. Blanco, P. Afanasiev, G. Berhault, D. Uzio, S. Loridant, Resonance Raman spectroscopy as a probe of the crystallite size of $MoS_2$ nanoparticles, Compt. Rendus Chem. 19 (2016) 1310–1314.

[44] M. Steichen, R. Djemour, L. Gütay, J. Guillot, S. Siebentritt, P.J. Dale, Direct synthesis of single-phase p-type SnS by electrodeposition from a dicyanamide ionic liquid at high temperature for thin film solar cells, J. Phys. Chem. C 117 (2013) 4383–4393.

[45] H. Hiroshi, Properties of GaN and related compounds studied by means of Raman scattering, J. Phys. Condens. Matter 14 (2002) R967.

[46] H. Grille, C. Schnittler, F. Bechstedt, Phonons in ternary group-III nitride alloys, Phys. Rev. B 61 (2000) 6091–6105.

[47] C. Bungaro, S.D. Gironcoli, Ab initio study of phonons in wurtzite $Al_xGa_{1-x}N$ alloys, Appl. Phys. Lett. 76 (2000) 2101–2103.

[48] J.A. Curcio, C.C. Petty, The near infrared absorption spectrum of liquid water, J. Opt. Soc. Am. 41 (1951) 302–304.

[49] L. Van Puyvelde, J. Lauwaert, P.F. Smet, S. Khelifi, T. Ericson, J.J. Scragg, D. Poelman, R. Van Deun, C. Platzer-Björkman, H. Vrielinck, Photo-luminescence investigation of $Cu_2ZnSnS_4$ thin film solar cells, Thin Solid Films 582 (2015) 146–150.

[50] A. Crovetto, R. Chen, R.B. Ettlinger, A.C. Cazzaniga, J. Schou, C. Persson, O. Hansen, Dielectric function and double absorption onset of monoclinic $Cu_2SnS_3$: origin of experimental features explained by first-principles calculations, Sol. Energy Mater. Sol. Cell. 154 (2016) 121–129.

[51] T. Raadik, M. Grossberg, J. Krustok, M. Kauk-Kuusik, A. Crovetto, R.B. Ettlinger, O. Hansen, J. Schou, Temperature dependent photoreflectance study of $Cu_2SnS_3$ thin films produced by pulsed laser deposition, Appl. Phys. Lett. 110 (2017) 261105.

[52] N. Aihara, H. Araki, K. Tanaka, Excitonic and band-to-band transitions in temperature-dependent optical absorption spectra of Cu2SnS3 thin films, Phys. Status Solidi B 255 (3) (2017), 1700304-n/a.

[53] S. Siebentritt, G. Rey, A. Finger, D. Regesch, J. Sendler, T.P. Weiss, T. Bertram, What is the bandgap of kesterite? Sol. Energy Mater. Sol. Cell 156 (2016) 126–129.

[54] J.K. Katahara, H.W. Hillhouse, Quasi-Fermi level splitting and sub-bandgap absorptivity from semiconductor photoluminescence, J. Appl. Phys. 116 (2014) 173504.

[55] R. Chen, C. Persson, Exploring the electronic and optical properties of $Cu_2Sn_{1-x}Ge_xS_3$ and $Cu_2Sn_{1-x}Si_xS_3$ (x = 0, 0.5, and 1), Phys. Status Solidi B 254 (2017) 1700111.

[56] L.L. Baranowski, P. Zawadzki, S. Christensen, D. Nordlund, S. Lany, A.C. Tamboli, L. Gedvilas, D.S. Ginley, W. Tumas, E.S. Toberer, A. Zakutayev, Control of doping in $Cu_2SnS_3$ through defects and alloying, Chem. Mater. 26 (2014) 4951–4959.

[57] F.I.K. Momma, VESTA 3 for three-dimensional visualization of crystal, volumetric and morphology data, J. Appl. Crystallogr. 44 (2011) 1272–1276.